

Elastic least-squares reverse time migration

Zongcai Feng¹ and Gerard T. Schuster¹

ABSTRACT

We use elastic least-squares reverse time migration (LSRTM) to invert for the reflectivity images of P- and S-wave impedances. Elastic LSRTM solves the linearized elastic-wave equations for forward modeling and the adjoint equations for backpropagating the residual wavefield at each iteration. Numerical tests on synthetic data and field data reveal the advantages of elastic LSRTM over elastic reverse time migration (RTM) and acoustic LSRTM. For our examples, the elastic LSRTM images have better resolution and amplitude balancing, fewer artifacts, and less crosstalk compared with the elastic RTM images. The images are also better focused and have better reflector continuity for steeply dipping events compared to the acoustic LSRTM images. Similar to conventional least-squares migration, elastic LSRTM also requires an accurate estimation of the P- and S-wave migration velocity models. However, the problem remains that, when there are moderate errors in the velocity model and strong multiples, LSRTM will produce migration noise stronger than that seen in the RTM images.

INTRODUCTION

Conventional seismic processing is based on the acoustic approximation. However, the real earth is viscoelastic and allows for the propagation of P- and S-waves. The S-waves are commonly recorded by multicomponent receivers in land or marine (ocean bottom) seismic experiments. For acoustic migration, the elastic characteristics of the wavefield, such as P-wave radiation patterns and mode-converted events, are treated as coherent noise rather than an additional source of information of the subsurface parameters (Sears et al., 2010).

For elastic imaging, elastic Kirchhoff migration and reverse time migration (RTM) are typically used for migrating multicomponent data. Elastic Kirchhoff migration (Kuo and Dai, 1984; Hokstad,

2000) calculates PP- and PS-traveltimes, and then it sums the multi-component data along the traveltimes moveout curves. It is equivalent to applying two acoustic Kirchhoff migrations after separating the PP- and PS-reflections according to the moveout differences in the PP- and PS-arrival times (Yan and Sava, 2008). Similarly, other conventional migration methods can be applied to PP- and PS-wave-fields after their separation. Usually, the P- and S-waves can be approximated by the vertical- and horizontal-component data (Granli et al., 1999) or separated by using approximations such as elastic potentials (Etgen, 1988; Zhe and Greenhalgh, 1997; Sun and McMechan, 2001; Stanton and Sacchi, 2014). The separation of P- and S-waves is not always accurate because it will generate crosstalk artifacts between the unseparated wave modes in the migration images (Du et al., 2012).

An alternative elastic-imaging method is elastic RTM, in which a numerical solution to the elastic-wave equation is used to extrapolate the P- and S-wave wavefields at the same time, without prior separation of wave modes. In this case, an imaging condition is used such as computing the ray-based excitation time of the reflection at the reflector (Chang and McMechan, 1987) or calculating the zero-lag crosscorrelation of the vector and scalar potentials (Yan and Sava, 2008; Du et al., 2012; Duan and Sava, 2015) to get the migration images. The benefit of elastic RTM is that it uses the correct kinematics to handle multicomponent data and migrates different wave modes to their correct subsurface positions (Lu et al., 2009; Jiao et al., 2012).

For least-squares migration, we seek the earth's reflectivity image from the seismic reflection data that minimizes the l_2 norm of the data residuals (Lailly, 1984; Tarantola, 1984; Chavent, 1999). It can be implemented with Kirchhoff's migration (Nemeth et al., 1999; Duquet et al., 2000) or phase-shift migration algorithms (Kuhl and Sacchi, 2003; Kaplan et al., 2010; Huang and Schuster, 2012). When implemented with the acoustic RTM method, acoustic least-squares reverse time migration (LSRTM) can be applied to acoustic data to improve its amplitude balancing and image resolution (Tang, 2009; Dai et al., 2012; Dai and Schuster, 2013; Zeng et al., 2014; Zhang et al., 2015), and it can be adapted to the viscoacoustic-wave equation (Dutta and Schuster, 2014; Dai et al., 2015) to compensate for

Manuscript received by the Editor 14 May 2016; revised manuscript received 26 October 2016; published online 16 February 2017.

¹King Abdullah University of Science and Technology, Department of Earth Science and Engineering, Thuwal, Saudi Arabia. E-mail: feng.zongcai@kaust.edu.sa; gerard.schuster@kaust.edu.sa.

© 2017 Society of Exploration Geophysicists. All rights reserved.

phase distortion and amplitude losses from attenuation. The results can be validated by comparing the observed traces to the synthetic pressure data generated by an acoustic- or viscoacoustic-wave equation. Such pressure data have neither a correct P-wave amplitude-variation-with-offset (AVO) effect (Virieux and Operto, 2009; Sears et al., 2010) nor S-wave events as generated in the elastic modeling or collected in the field. Recently, Stanton and Sacchi (2015) combine wavefield separation and split-step wave-equation migration to improve the ability of least-squares migration to fit elastic data. We now adapt LSRTM to the elastic-wave equation to directly take care of this elastic characteristic.

The theory of elastic waveform inversion dates back to the works of Tarantola (1986) and Mora (1987). It is a nonlinear waveform inversion method that iteratively updates the background elastic parameters using transmission and reflection data (Mora, 1988). We now use the elastic gradient formula of waveform inversion (Crase et al., 1990) to compute the least-squares migration image (Nemeth et al., 1999; Duquet et al., 2000; Valenciano, 2006), and we do not update the smooth background velocity. This method is referred to as elastic LSRTM.

In our elastic LSRTM algorithm, we choose to invert for the reflectivity images of P- and S-wave impedances but not the P- and S-wave velocities or the Lamé parameters λ and μ for two reasons (Tarantola, 1986). First, the P- and S-wave impedances give scattering radiation patterns that are more dissimilar than those associated with the Lamé parameters λ and μ . Such parameterization reduces the crosstalk due to the weak coupling between parameters and speeds up the convergence. Second, when the P- and S-wave impedances are selected, the density perturbations scatter little energy at a short aperture. This gives reflectivity images with better quality, even though density is not inverted for. After choosing the elastic parameters in inversion, elastic LSRTM uses a linearized iterative approach to reduce the coupling effect between elastic parameters, which is similar to that described in Anikiev et al. (2013). Here, the scattering radiation patterns are referred to as the scattering characteristics of elastic waves (Wu and Aki, 1985; Tarantola, 1986). However, the crosstalk caused by the coupling between parameters in multiparameter inversion is still a problem.

In this paper, we use the elastic-wave equations for wavefield extrapolation and use the linearized least-squares inversion method (Lailly, 1984) to invert for the reflectivity images of the P- and S-wave impedances. For elastic LSRTM, the linearized elastic modeling operator is based on the perturbations of the Lamé parameters λ and μ . We derive the adjoint equations and imaging conditions to calculate the gradients with respect to λ and μ . The gradients are then transformed into gradients with respect to updating the reflectivity images of the P- and S-wave impedances. Numerical tests on synthetic data show that elastic LSRTM provides P- and S- images with fewer artifacts, better amplitude balancing, and higher resolution than does elastic RTM if the velocity model is well-known and the multiples are not too strong. In addition, crosstalk noise between the P- and S-images can be mitigated by the least-squares iterations for our examples. When compared with acoustic LSRTM, elastic LSRTM images are more focused and have fewer artifacts because LSRTM accurately accounts for the P-wave radiation pattern. In addition, elastic LSRTM improves the imaging of steeply dipping structures using S-wave reflections. The disadvantage is that elastic LSRTM is an order-of-magnitude more expensive than acoustic LSRTM, relies on an accurate estimation of the P- and S-wave migration velocity models, and it is sensitive to the presence of strong multiples.

This paper is organized into five sections. After the Introduction, the second section describes the theory and the implementation of elastic LSRTM. Numerical results on the synthetic and field data are presented in the third section. The field data are from a crosswell survey in West Texas, where there is good coverage in the source and receiver distributions. Finally, discussions and conclusions are presented in the last two sections.

THEORY OF ELASTIC LEAST-SQUARES REVERSE TIME MIGRATION

The 2D velocity-stress elastic-wave equation can be written as (Levander, 1988)

$$\begin{aligned} \rho \frac{\partial u_x}{\partial t} - \left(\frac{\partial \sigma_{xx}}{\partial x} + \frac{\partial \sigma_{xz}}{\partial z} \right) &= 0, \\ \rho \frac{\partial u_z}{\partial t} - \left(\frac{\partial \sigma_{zz}}{\partial z} + \frac{\partial \sigma_{xz}}{\partial x} \right) &= 0, \\ \frac{\partial \sigma_{xx}}{\partial t} - \lambda \left(\frac{\partial u_x}{\partial x} + \frac{\partial u_z}{\partial z} \right) - 2\mu \frac{\partial u_x}{\partial x} &= S_{xx}, \\ \frac{\partial \sigma_{zz}}{\partial t} - \lambda \left(\frac{\partial u_x}{\partial x} + \frac{\partial u_z}{\partial z} \right) - 2\mu \frac{\partial u_z}{\partial z} &= S_{zz}, \\ \frac{\partial \sigma_{xz}}{\partial t} - \mu \left(\frac{\partial u_x}{\partial z} + \frac{\partial u_z}{\partial x} \right) &= 0, \end{aligned} \quad (1)$$

where u_x and u_z are the horizontal- and vertical-particle velocities, σ_{xx} , σ_{zz} , and σ_{xz} are the stresses, S_{xx} and S_{zz} denote the source time histories of “ xx ” and “ zz ” stress components, respectively, λ and μ are the Lamé parameters, and ρ is the density. The P-wave velocity is given by $V_P = \sqrt{(\lambda + 2\mu)/\rho}$ and the S-wave velocity is $V_S = \sqrt{\mu/\rho}$. The P-wave impedance is given by $I_P = \rho V_P = \sqrt{\rho(\lambda + 2\mu)}$ and the S-wave impedance is $I_S = \rho V_S = \sqrt{\rho\mu}$.

Let λ_0 and μ_0 be the background medium parameters. Perturbing them by $\delta\lambda$ and $\delta\mu$, respectively, while keeping ρ unchanged, gives the new medium parameters as

$$\lambda = \lambda_0 + \delta\lambda, \quad \mu = \mu_0 + \delta\mu. \quad (2)$$

The perturbed wavefields can thus be written as

$$\begin{aligned} \rho \frac{\partial \delta u_x}{\partial t} - \left(\frac{\partial \delta \sigma_{xx}}{\partial x} + \frac{\partial \delta \sigma_{xz}}{\partial z} \right) &= 0, \\ \rho \frac{\partial \delta u_z}{\partial t} - \left(\frac{\partial \delta \sigma_{zz}}{\partial z} + \frac{\partial \delta \sigma_{xz}}{\partial x} \right) &= 0, \\ \frac{\partial \delta \sigma_{xx}}{\partial t} - \lambda \left(\frac{\partial \delta u_x}{\partial x} + \frac{\partial \delta u_z}{\partial z} \right) - 2\mu \frac{\partial \delta u_x}{\partial x} &= \delta\lambda \left(\frac{\partial u_x}{\partial x} + \frac{\partial u_z}{\partial z} \right) + 2\delta\mu \frac{\partial u_x}{\partial x}, \\ \frac{\partial \delta \sigma_{zz}}{\partial t} - \lambda \left(\frac{\partial \delta u_x}{\partial x} + \frac{\partial \delta u_z}{\partial z} \right) - 2\mu \frac{\partial \delta u_z}{\partial z} &= \delta\lambda \left(\frac{\partial u_x}{\partial x} + \frac{\partial u_z}{\partial z} \right) + 2\delta\mu \frac{\partial u_z}{\partial z}, \\ \frac{\partial \delta \sigma_{xz}}{\partial t} - \mu \left(\frac{\partial \delta u_x}{\partial z} + \frac{\partial \delta u_z}{\partial x} \right) &= \delta\mu \left(\frac{\partial u_x}{\partial z} + \frac{\partial u_z}{\partial x} \right). \end{aligned} \quad (3)$$

In the context of least-squares migration, the variables in equation 3 are related to the matrix-vector operation $\mathbf{d} = \mathbf{Lm}$ (Nemeth et al., 1999). Here, $\mathbf{d} = (\delta u_x, \delta u_z)^T$ represents the Born-modeled particle

velocities, \mathbf{L} is a linear modeling operator, and $\mathbf{m} = (\delta\lambda, \delta\mu)^T$ is the perturbation of the Lamé parameters.

For elastic LSRTM, we seek to find the perturbed wavefields related to the reflectivity images of P- and S-wave impedances defined as $(\delta m_P, \delta m_S)^T = (\delta I_P/I_P, \delta I_S/I_S)^T$. To calculate the perturbed wavefields, we substitute the following equation into equation 3:

$$\delta\lambda = 2(I_P^2 \delta m_P - 2I_S^2 \delta m_S)/\rho, \quad \delta\mu = 2I_S^2 \delta m_S/\rho. \quad (4)$$

Inverting for these parameters has two benefits. First, they closely resemble the reflectivity distributions. In the acoustic case, $\delta I_P/I_P$ is usually defined as the normal reflectivity (reflectivity at normal incidence). Second, compared with the P-wave impedance δI_P and S-wave impedance δI_S , they have better scaling, so they are similar in strength to the wavefield.

Acoustic least-squares migration assumes that the scattering radiation pattern of the P-wave event is direction independent, as shown in the PP-radiation pattern for δI_P in Figure 1a. It cannot explain the pressure field that is also contributed by other parameter perturbations, such as δI_S , as shown in the PP-radiation pattern for δI_S , which is direction dependent. It also neglects the S-wave events, such as the PS-scattering. Using acoustic least-squares migration for migrating an elastic wavefield will generate artifacts, especially when data from large offsets are used.

The adjoint equations for equation 1 can be derived using the adjoint-state method (Plessix, 2006):

$$\begin{aligned} \frac{\partial}{\partial t}(\rho\hat{u}_x) - \frac{\partial}{\partial x}((\lambda + 2\mu)\hat{\sigma}_{xx}) - \frac{\partial}{\partial x}(\lambda\hat{\sigma}_{zz}) \\ - \frac{\partial}{\partial z}(\mu\hat{\sigma}_{xz}) = -\Delta d_x(\mathbf{x}_g, t; \mathbf{x}_s), \\ \frac{\partial}{\partial t}(\rho\hat{u}_z) - \frac{\partial}{\partial z}((\lambda + 2\mu)\hat{\sigma}_{zz}) - \frac{\partial}{\partial z}(\lambda\hat{\sigma}_{xx}) \\ - \frac{\partial}{\partial x}(\mu\hat{\sigma}_{xz}) = -\Delta d_z(\mathbf{x}_g, t; \mathbf{x}_s), \\ \frac{\partial\hat{\sigma}_{xx}}{\partial t} - \frac{\partial\hat{u}_x}{\partial x} = 0, \\ \frac{\partial\hat{\sigma}_{zz}}{\partial t} - \frac{\partial\hat{u}_z}{\partial z} = 0, \\ \frac{\partial\hat{\sigma}_{xz}}{\partial t} - \frac{\partial\hat{u}_x}{\partial z} - \frac{\partial\hat{u}_z}{\partial x} = 0, \end{aligned} \quad (5)$$

where $(\hat{u}_x, \hat{u}_z, \hat{\sigma}_{xx}, \hat{\sigma}_{zz}, \hat{\sigma}_{xz})$ are the adjoint-state variables of the state variables $(u_x, u_z, \sigma_{xx}, \sigma_{zz}, \sigma_{xz})$, respectively. For elastic LSRTM, $\Delta d_x(\mathbf{x}_g, t; \mathbf{x}_s)$ and $\Delta d_z(\mathbf{x}_g, t; \mathbf{x}_s)$ represent the data residual between the predicted and observed vertical- and horizontal-particle-velocity data at every iteration.

The perturbation in the image $\delta\mathbf{m}$ is related to the perturbations of the Lamé parameters λ and μ , which can be obtained by zero-lag crosscorrelation of the adjoint fields from equation 5 with the background wavefields from equation 1:

$$\begin{aligned} \delta\mathbf{m} &= \begin{pmatrix} -\frac{\partial e}{\partial \lambda} \\ -\frac{\partial e}{\partial \mu} \end{pmatrix} \\ &= \begin{pmatrix} -\int_0^T \left(\frac{\partial u_x}{\partial x} + \frac{\partial u_z}{\partial z} \right) (\hat{\sigma}_{xx} + \hat{\sigma}_{zz}) dt \\ -\int_0^T 2 \left(\frac{\partial u_x}{\partial x} \hat{\sigma}_{xx} + \frac{\partial u_z}{\partial z} \hat{\sigma}_{zz} \right) + \left(\frac{\partial u_x}{\partial z} + \frac{\partial u_z}{\partial x} \right) \hat{\sigma}_{xz} dt \end{pmatrix}, \end{aligned} \quad (6)$$

where e is the misfit function defined in equation 7, and $(\partial e / \partial \lambda)$ and $(\partial e / \partial \mu)$ are the gradients with respect to perturbations in λ and μ . Their derivation is shown in Appendix A. Equations 5 and 6 are equivalent to the gradient operation $\mathbf{g} = \mathbf{L}^T \Delta \mathbf{d}$ used in conventional least-squares migration (Nemeth et al., 1999). The algorithm for numerical implementation of elastic LSRTM is discussed in the next subsection.

Elastic least-squares reverse time migration algorithm

Elastic LSRTM is implemented by a preconditioned conjugate gradient method (Nocedal and Wright, 1999) based on the follow-

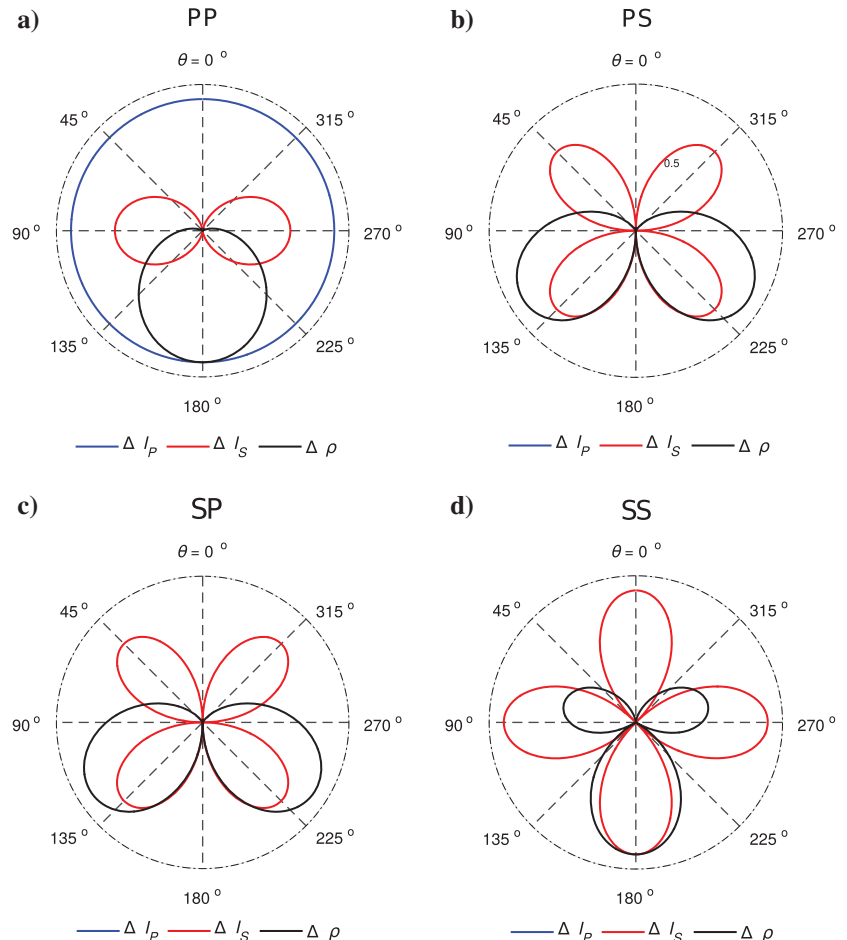


Figure 1. Scattering radiation patterns of the P- and S-wave impedances as well as density for four scattering modes: (a) PP, (b) PS, (c) SP, and (d) SS, in which all the plots are normalized, so that the maximum amplitudes have the same value. The scattering radiation patterns are plotted as polar coordinates as a function of the scattering (or aperture) angle. Note that a P-wave impedance perturbation generates only PP-diffraction with an isotropic diffraction pattern (Prieux et al., 2013).

ing steps. Our work flow is similar to that of Dutta and Schuster (2014), except the parameters and data are multicomponent. In this work, source-side illumination (Plessix and Mulder, 2004) is used as the diagonal preconditioner \mathbf{C} :

- Form the misfit function ϵ as

$$\epsilon = \frac{1}{2} \|\mathbf{Lm}^{(i+1)} - \mathbf{d}^{\text{obs}}\|^2, \quad (7)$$

where \mathbf{L} represents a linear modeling operator and $\mathbf{Lm}^{(i+1)}$ is the predicted data given by the solution to equation 3; \mathbf{d}^{obs} represents the recorded vertical- and horizontal-particle-velocity seismograms, \mathbf{m} represents the perturbations of the Lamé parameters computed from the reflectivity images of P- and S-wave impedances using equation 4, and i represents the iteration index.

- Compute the gradient

$$\mathbf{g}^{(i+1)} = \mathbf{L}^T (\mathbf{Lm}^{(i+1)} - \mathbf{d}^{\text{obs}}) = \mathbf{L}^T \Delta \mathbf{d}^{(i+1)}, \quad (8)$$

where $\Delta \mathbf{d}$ represents the data residual for the predicted and observed data, which is back propagated using the adjoint equations in equation 5. The adjoint wavefields are crosscorrelated with the background fields, given in equation 1, to give the gradients related to the Lamé parameters in equation 6 at each iteration. The gradients are then used to calculate the gradients related to the reflectivity images by

$$\frac{\partial \epsilon}{\partial m_P} = 2V_P I_P \frac{\partial \epsilon}{\partial \lambda}, \quad \frac{\partial \epsilon}{\partial m_S} = 2V_S I_S \left(-2 \frac{\partial \epsilon}{\partial \lambda} + \frac{\partial \epsilon}{\partial \mu} \right). \quad (9)$$

The gradient transformation for reflectivity images is similar to the transformation for P- and S-wave impedances (Crane et al., 1990), except it is scaled by the background P- and S-wave impedances.

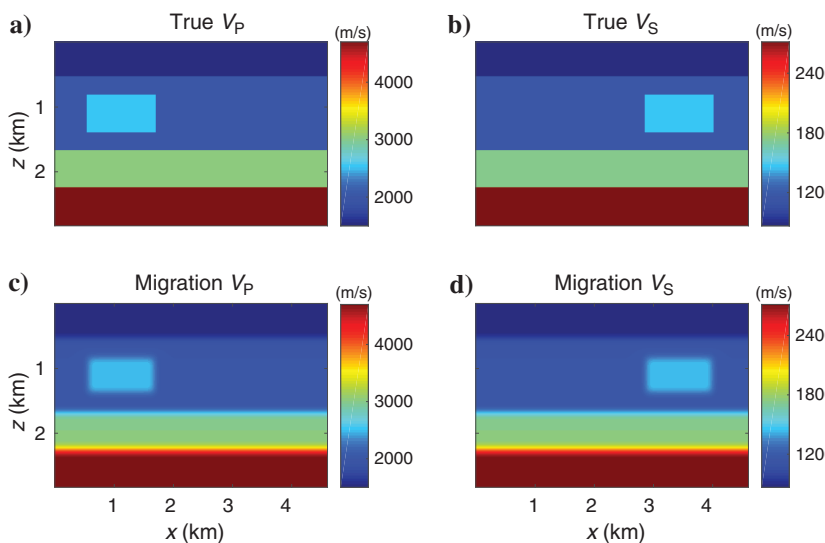


Figure 2. A layered model: (a) true V_P , (b) true V_S , (c) migration V_P , and (d) migration V_S models.

- Update the gradient related to reflectivity images using the conjugate gradient formula as

$$\mathbf{dk}^{(i+1)} = \mathbf{Cg}^{(i+1)} + \beta \mathbf{dk}^{(i)}, \quad (10)$$

where β is given by

$$\beta = \frac{(\mathbf{g}^{(i+1)})^T \mathbf{Cg}^{(i+1)}}{(\mathbf{g}^{(i)})^T \mathbf{Cg}^{(i)}}. \quad (11)$$

In this work, we use the sum of the square of the horizontal- and vertical-particle velocities for source-side illumination

$$[\mathbf{C}]_{ii} = 1 / \int_0^T (u_x(\mathbf{x}_i)^2 + u_z(\mathbf{x}_i)^2) dt. \quad (12)$$

where $[\mathbf{C}]_{ii}$ indicates the i th diagonal term of \mathbf{C} and \mathbf{x}_i indicates the wavefield location.

- Compute the step length α as

$$\alpha = \frac{(\mathbf{dk}^{(i+1)})^T \mathbf{g}^{(i+1)}}{(\mathbf{Ldk}^{(i+1)})^T (\mathbf{Ldk}^{(i+1)})}. \quad (13)$$

- Iteratively update the reflectivity images as

$$\mathbf{m}^{(i+2)} = \mathbf{m}^{(i+1)} - \alpha \mathbf{dk}^{(i+1)}, \quad (14)$$

until the length of the residual vector falls below a specified threshold.

NUMERICAL RESULTS

The application of elastic LSRTM is now demonstrated with synthetic and field data examples. The synthetic examples are for three land models: (1) a layered model with different P- and S-wave velocity anomalies, (2) a portion of the Marmousi2 model, and (3) a modified cross section of the SEG/EAGE salt model. The field data are from a crosswell experiment in McElroy, Texas.

In the synthetic examples, the observed 2C data are generated by an $O(2, 8)$ time-space-domain staggered-grid solution of the elastic-wave equations in equation 1 without a free-surface condition. The data are then migrated using elastic RTM and elastic LSRTM for the reflectivity images of P- and S-wave impedances. Here, the reflectivity images of the P- and S-waves are denoted as the P- and S-images, respectively. The elastic RTM refers to the first iteration of elastic LSRTM. Source-side illumination is used as the preconditioning factor during the least-squares iterations for elastic LSRTM. The elastic RTM and acoustic LSRTM results are also illumination compensated.

Layered velocity model

We first demonstrate the advantages of elastic LSRTM using the flat-layered model in Figure 2 with shallow anomalies. The density is homo-

geneous and equal to 1 g/cm^3 ; thus, the P- and S-wave impedances as well as density models are not shown here. To generate the synthetic data, equation 1 is solved for 92 shots evenly spaced at 50 m on the surface. Here, 230 receivers are evenly distributed at 20 m intervals on the surface. The P-wave point source uses a Ricker wavelet with a 7.5 Hz peak frequency, and the total recording time is 5.6 s.

Figure 3 compares the elastic RTM and LSRTM images. In both cases, the S-images have higher resolution than the P-images because of the shorter wavelength of S-waves. The elastic LSRTM images have fewer artifacts, better amplitude balancing, and higher resolution compared with the elastic RTM images. In addition, the P- and S-images of elastic RTM contain false reflectivity images of P- and S-wave velocity anomalies. Note that the crosstalk noise exists at the flat-layered interfaces in the images, but it overlaps the true images. The crosstalk problem in elastic RTM is mitigated by elastic LSRTM.

Source-type test

In our previous synthetic example, we used a P-wave source, which is common in elastic migration or inversion of marine (ocean-bottom) data, including synthetic data (Lu et al., 2009; Guasch et al., 2012; Raknes and Arntsen, 2014) and field data (Sears et al., 2008, 2010; Jiao et al., 2012). The recorded wavefield thus contains only PP- and converted PS-reflections. If the correct velocity models are used, the cross-correlation of the source- and receiver-side wavefields relocates the reflection events back to their place of origin along the reflecting interfaces, even though there is crosstalk generated by the coupling between parameters. However, if the source contains P- and S-waves, the recorded data will contain PP-, PS-, SS-, and SP-reflections. In this case, the crosscorrelation between different wave modes will generate migration artifacts between different wave modes.

We now use the same layered velocity model in the synthetic example, except now only 23 shots are used, with a shot spacing of 200 m. The elastic LSRTM images using a normal stress source σ_{zz} are shown in Figure 4a and 4b. The images contain obvious wave-mode crosstalk noise especially in the shallow part of the P-image, compared with the elastic LSRTM images using the P-wave source shown in Figure 4c and 4d. This wave-mode crosstalk is difficult to eliminate with more iterations of elastic LSRTM. However, if a denser distribution of shots is used, the wave-mode crosstalk is mitigated as shown in Figure 4e and 4f. This is because the location of the wave-mode crosstalk and artifacts varies with shot location, and therefore, stacking the images cancels the artifacts for a dense shot distribution.

Marmousi2 velocity model

We also demonstrate the advantages of elastic LSRTM using a portion of the Marmousi2 model with a homogeneous solid layer added on the top. Figure 5a, 5c, and 5e shows the true P- and S-wave velocities as well as density models, respectively. The models for migration are shown in Figure 5b, 5d, and 5f. The true P- and S-wave impedance models, calculated from the true velocity and

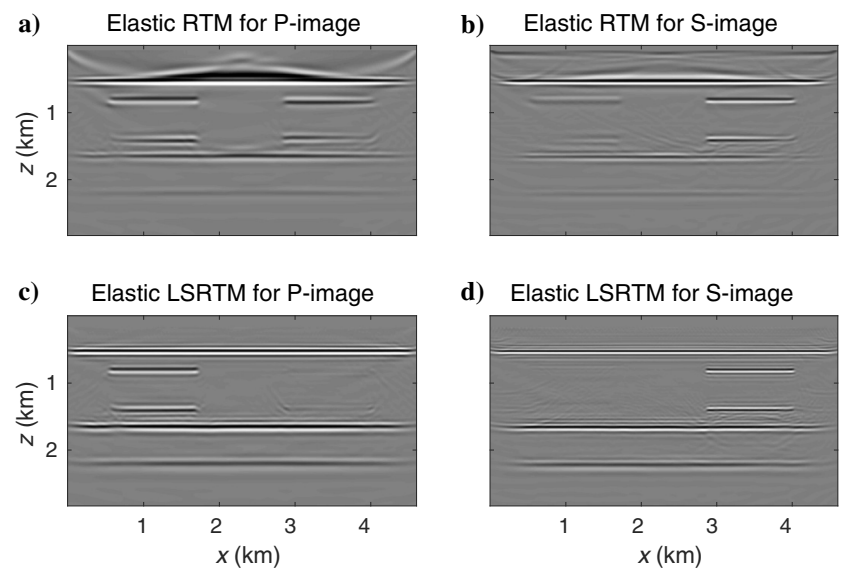


Figure 3. Migration images of the layered model: elastic RTM reflectivity images of (a) I_P and (b) I_S , elastic LSRTM reflectivity images of (c) I_P and (d) I_S .

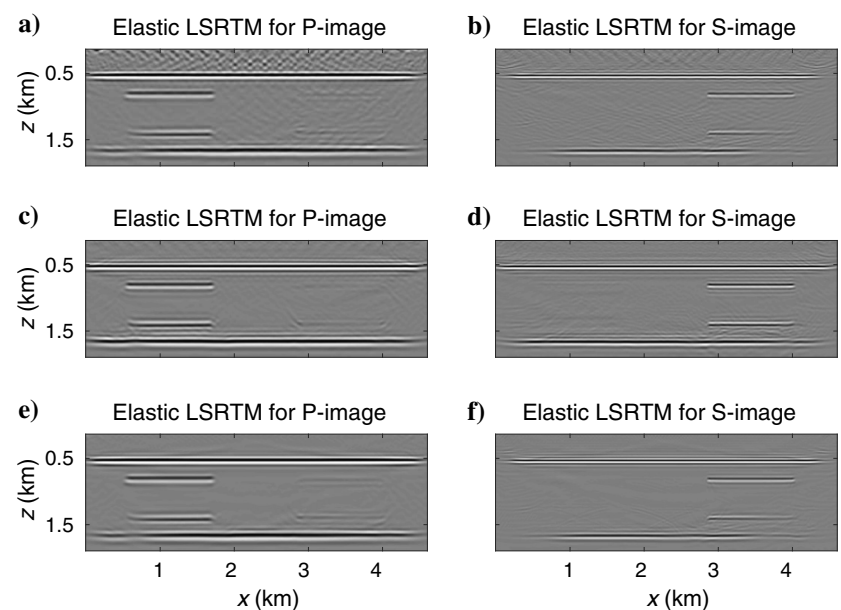


Figure 4. Elastic LSRTM images with 23 shots using (a and b) a normal stress source, (c and d) a P-wave source, and (e and f) using 92 shots with normal stress sources. The deeper parts of the images are almost identical, and thus are not shown here.

density models, are shown in Figure 6a and 6b, respectively. The 478 shots are evenly spaced at 12.5 m, and the 1195 receivers are evenly distributed at 5.0 m intervals on the surface. The P-wave point source uses a Ricker wavelet with a 30-Hz peak frequency, and the total recording time is 3 s.

The elastic RTM and LSRTM images are displayed in Figure 7. Similar to the previous example, the S-images have higher resolution than the P-images. The elastic LSRTM images also have fewer artifacts, better amplitude balancing, and higher resolution compared with elastic RTM. In addition, the false sand structure appearing in the RTM P-image is much weaker in the LSRTM P-image (shown by the black arrows in Figure 7 and in the magnified views in Figure 8). The S-images for elastic RTM and LSRTM show a consistent structure in the sand layer.

Figure 5. A portion of the Marmousi2 model: (a) true V_P , (b) migration V_P , (c) true V_S , (d) migration V_S , (e) true density, and (f) migration density models.

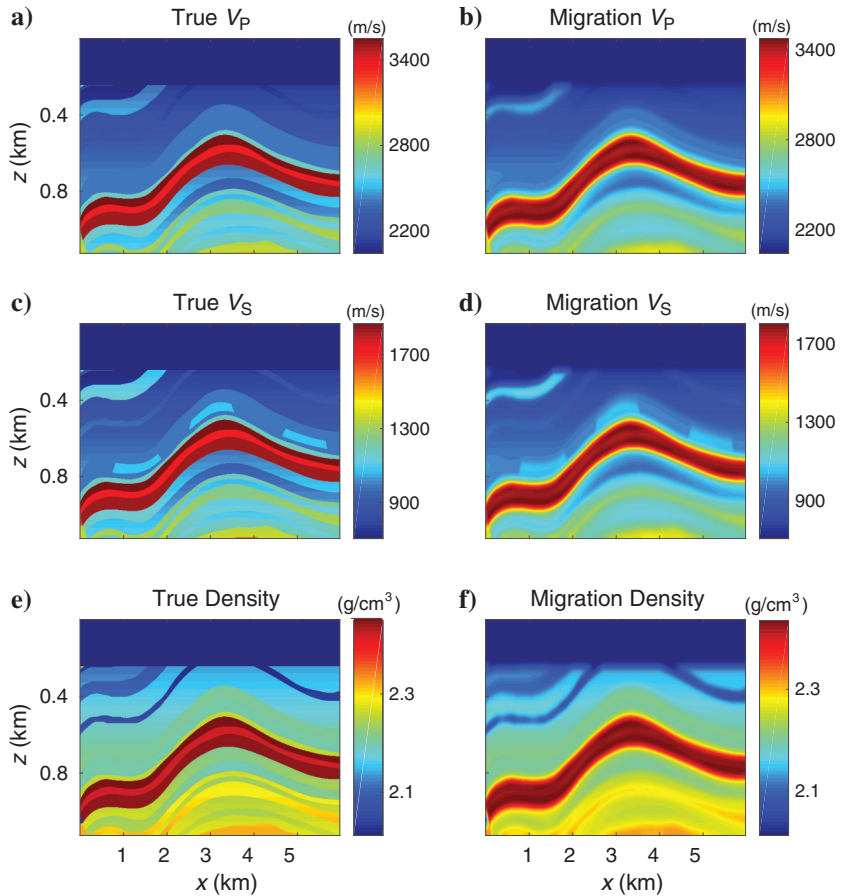
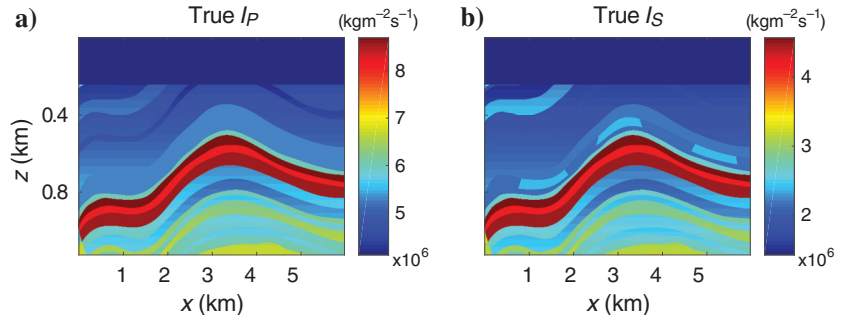


Figure 6. A portion of the Marmousi2 model: (a) true I_P and (b) true I_S models calculated from the true V_P , V_S , and density models.



SEG/EAGE salt model

Elastic LSRTM is now tested on the SEG/EAGE salt model for comparison with acoustic LSRTM. Figure 9a and 9b shows the true P- and S-wave velocity models, respectively. The S-wave velocity is obtained by scaling the P-wave velocity by half. The density is homogeneous and equal to 1 g/cm^3 ; thus, the P- and S-wave impedances as well as density models are not shown here. The P- and S-wave velocity models for migration are shown in Figure 9c and 9d, respectively. Equation 1 is solved to generate traces with two particle-velocity components for elastic LSRTM and the pressure component (the negative of the average of the normal stress components) for acoustic LSRTM. The 258 shots are evenly spaced at 50 m, and 644 receivers are evenly distributed at 20 m intervals on

the surface. The P-wave point source uses a Ricker wavelet with a 7.5 Hz peak frequency, and the total recording time is 5 s.

Acoustic and elastic LSRTM images are displayed in Figure 10. The elastic LSRTM images show better resolution and fewer artifacts. Profiles of the true and migration P-reflectivity images at $x = 0.80$ km are shown in Figure 11. Although acoustic LSRTM image achieves the same resolution as the P-image of elastic LSRTM, it generates significant wiggle-shape artifacts around the true reflecting interfaces. In addition, elastic LSRTM produces better images of the salt and subsalt structures compared with the acoustic LSRTM image. The magnified views in Figure 12 show that in elastic LSRTM, the images of the salt interface are more continuous and distinct. The magnified views in Figure 13 show that elastic LSRTM improves the subsalt imaging, especially along the steeply dipping events in the S-image.

LSRTM provides more accurate images than acoustic LSRTM because of two fundamental limitations in migrating elastic data with the acoustic-wave equation: the amplitude of the reflections and the geometry of the converted-wave raypaths. Acoustic LSRTM, although kinematically correct, fails to invert for a reflectivity image that best predicts the amplitude of pressure data generated in an elastic medium, as shown in Figure 11. This is because the acoustic-wave equation incorrectly models the P-wave wavefield by ignoring the AVO effect (Virieux and Operto, 2009; Sears et al., 2010). This P-wave amplitude error will generate artifacts in acoustic least-squares migration. This problem can be mitigated by applying specific waveform-inversion data processing designed to account for the amplitude errors introduced by acoustic modeling (Ravaut et al., 2004; Brenders and Pratt, 2007; Virieux and Operto, 2009), or using a crosscorrelation objective function for acoustic least-squares migration (Zhang et al., 2013; Dutta et al., 2014b; Sinha and Schuster, 2015).

Another reason of better imaging is that elastic LSRTM can migrate different wave-mode events, especially the converted waves,

into the proper position. For highly dipping events, the PP-reflections may not be recorded due to the limited recording aperture, whereas the PS-reflections, which have smaller reflection angles, are easier to record and use for migration (Stewart et al., 2002, 2003), as shown in Figure 14. In elastic LSRTM, the PS-reflections mainly contribute to construct the S-image, which helps to identify complex structures. However, the elastic LSRTM S-image is noisier than the elastic LSRTM P-image, as shown in Figure 10. This is because the S-image uses both the P- and S-reflections whereas the P-image only uses the P-reflections, according to the scattering radiation pattern shown in Figure 1.

McElroy crosswell field data

Elastic LSRTM is now applied to the McElroy crosswell data (Harris et al., 1995; Zhou et al., 1997). The source and receiver wells are 152 m deep and are separated by 56 m. Two hundred and one shots are evenly distributed at a depth interval of 0.76 m from 0 to 152 m in the source well, and the receiver well has 178 receivers placed at a depth interval of 0.76 m between the depths 11.4 and 146 m. The data were recorded with a sampling interval of 0.2 ms for a total recording time of 0.05 s.

A 200–1400 Hz band-pass filter is applied to the field data to filter out the high- and low-frequency noise, and a median filter is applied to the common-shot gathers to filter out the tube waves generated in the source and receiver wells. Figure 15 shows a common-shot gather before and after data processing. The elastic P- and S-wave velocity tomograms (Zhou et al., 1997) shown in Figure 16 are used as the migration velocity models for the elastic LSRTM. The source and receiver wells are located at $x = 0$ and 56 m, respectively. The data are resampled at the time interval of 0.01 ms, and the direct P-waves are muted out before migration. The borehole effects (Zhou et al., 1997) are accounted for by adjusting the elastic LSRTM algorithm with the following procedure:

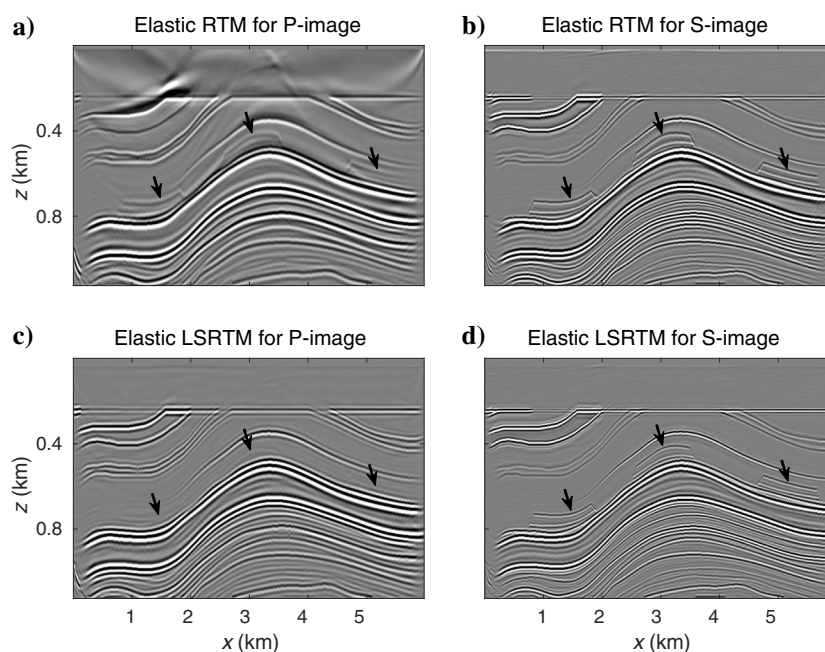


Figure 7. Migration images of the Marmousi2 model: elastic RTM reflectivity images of (a) I_P and (b) I_S , elastic LSRTM reflectivity images of (c) I_P and (d) I_S .

- The data contain strong S-wave events, such as SS- and SP-reflections (Harris et al., 1995; Zhou et al., 1997), and thus, the P-wave source is no longer suitable. We use an analytical source (White and Lessenger, 1988; Kurkjian et al., 1992; Zhou et al., 1997):

$$S_{xx}(t) = -2\pi a^2 \alpha_T \frac{\alpha^2}{\beta^2} S(t),$$

$$S_{zz}(t) = -2\pi a^2 \alpha_T \frac{\alpha^2}{\beta^2} S(t) + 4\pi a^2 \alpha_T S(t), \quad (15)$$

Figure 8. Magnified views showing the sand structure in Figure 7, in which all the images have been normalized. (a and b) True reflectivity images used only for comparison, (c and d) elastic RTM images, and (d and e) elastic LSRTM images.

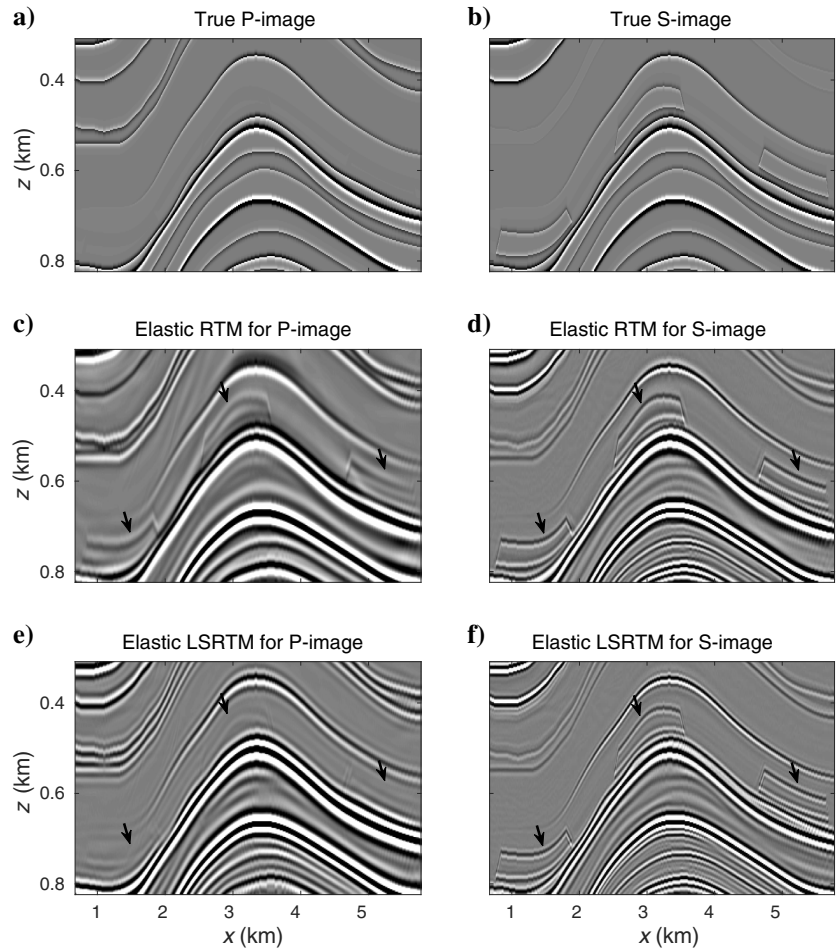
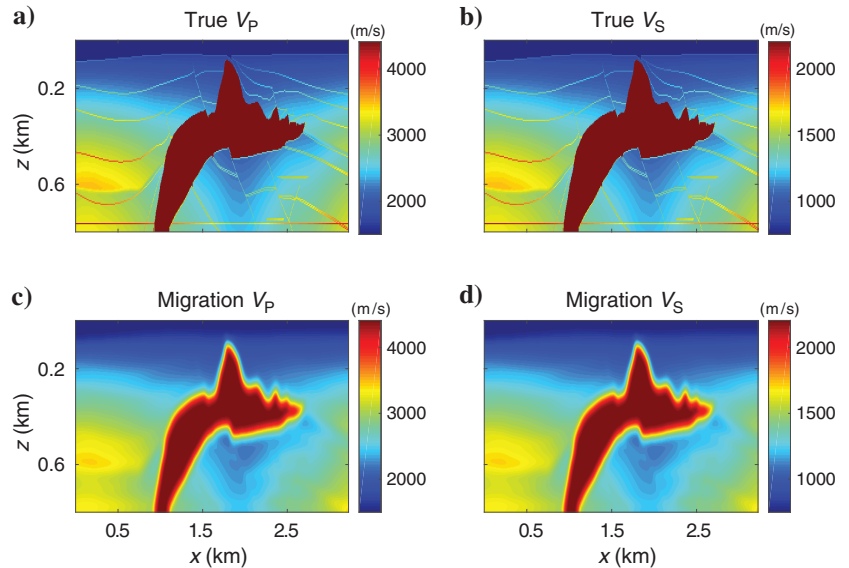


Figure 9. The SEG/EAGE salt models: (a) true V_P , (b) true V_S , (c) migration V_P , and (d) migration V_S models.



where α and β are the P- and S-wave velocities, respectively. The factor $2\pi a^2 \alpha_T$ can be ignored when doing forward modeling because it merely scales the migration images. A Ricker wavelet with a 1200-Hz peak frequency is used to approximate $S(t)$ in equation 15.

- The pressure field generated in the receiver well can be approximated from the stress components on the well wall by (White and Lessenger, 1988; Zhou et al., 1997)

$$P = K(\sigma_{xx} - v\sigma_{zz}), \quad (16)$$

where K is an unknown scaling factor that can be ignored, and v is the Poisson's ratio approximated from the velocity tomograms. The pressure residual is calculated by

$$\Delta \mathbf{d} = P - P^{\text{obs}}, \quad (17)$$

where P^{obs} is the pressure recorded by the hydrophones in the receiver well.

- The back-propagation of the pressure residual uses the adjoint operator in equation 16:

$$\Delta \mathbf{d}^{\text{adj}} = \begin{pmatrix} \Delta \sigma_{xx} \\ \Delta \sigma_{zz} \end{pmatrix} = \begin{pmatrix} 1 \\ -v \end{pmatrix} K(P - P^{\text{obs}}). \quad (18)$$

This equation transforms the pressure residual to a stress residual, and then $\mathbf{g} = \mathbf{L}^T \Delta \mathbf{d}^{\text{adj}}$ is used to calculate the gradients in elastic LSRTM.

The elastic RTM and LSRTM images are shown in Figure 17. The P-image computed by elastic LSRTM has better amplitude balancing and higher resolution compared with the P-image calculated with elastic RTM. Elastic LSRTM also improves the continuity of the reflectors close to the wells. Other structures become more noticeable in the P-image of elastic LSRTM, especially in the red and blue boxes in Figure 17. Magnified views of the red and blue boxes

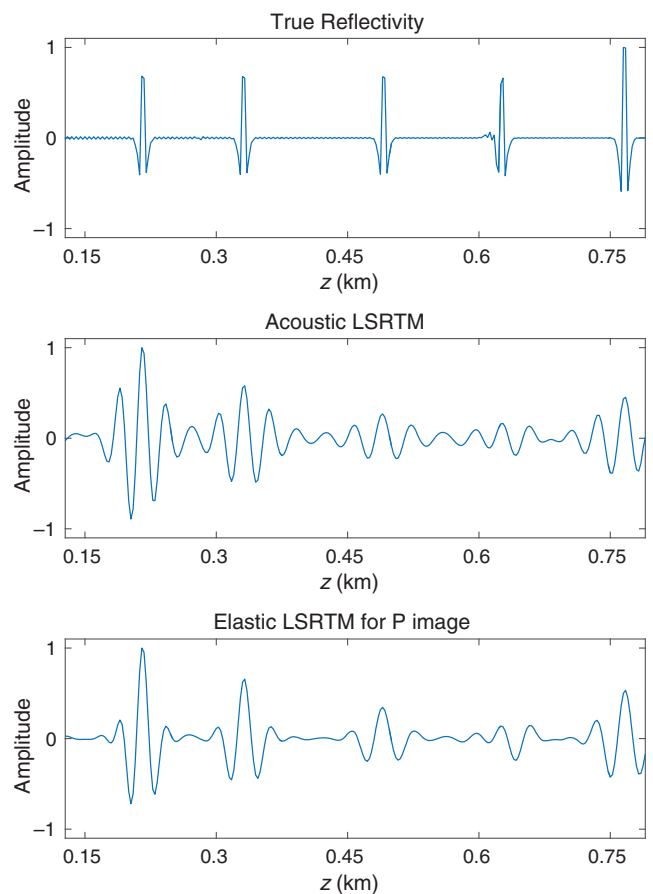


Figure 11. Profiles from the (a) true reflectivity image for I_P , (b) acoustic LSRTM image, and (c) elastic LSRTM reflectivity image for I_P at 0.80 km in the x -direction, in which the amplitudes have been normalized.

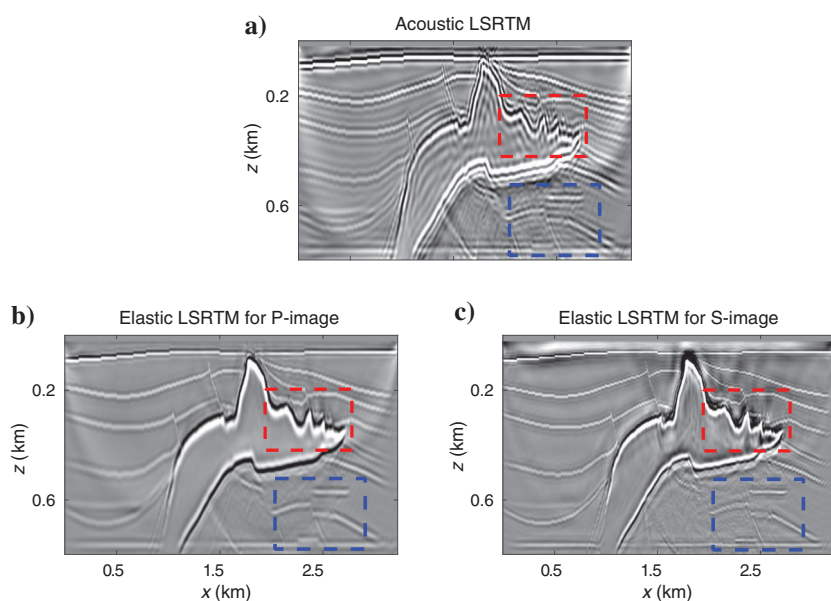


Figure 10. Migration images of the SEG/EAGE salt model: (a) acoustic LSRTM image, elastic LSRTM reflectivity images for (b) I_P and (c) I_S .

are shown in Figure 18. To verify the accuracy of the elastic LSRTM images, the sonic logs are compared with the elastic RTM and LSRTM image reflectivity profiles at the receiver well, as shown in Figure 19. The reflectivity profiles are taken 2 m away from the well at the depth range of the red and blue boxes. Figure 19 shows an acceptable match between the sonic logs and elastic LSRTM image reflectivity profiles, and the elastic LSRTM P-image reveals a more accurate reflectivity profile than that taken from the elastic RTM P-image.

The S-image of elastic LSRTM has no significant improvement, except for a slight amplitude balancing compared with elastic RTM, which is also shown in the reflectivity profiles. We think this is mainly caused by inaccurate estimations of the source radiation patterns and S-wave migration velocity, and by not taking into account attenuation effects in the elastic LSRTM algorithm (Zhou et al.,

Figure 12. Magnified views of the red boxes showing the salt interface in Figure 10.

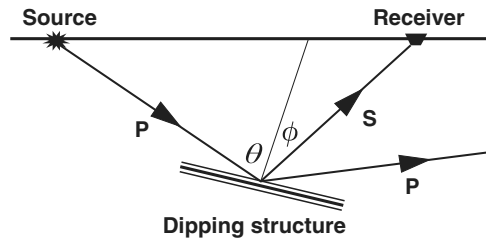


Figure 14. Schematic diagrams of reflection wavepaths from dipping structures for unconverted PP- and converted PS-reflections, in which the reflected S-wave angle ϕ is smaller than the incident P-wave angle θ .

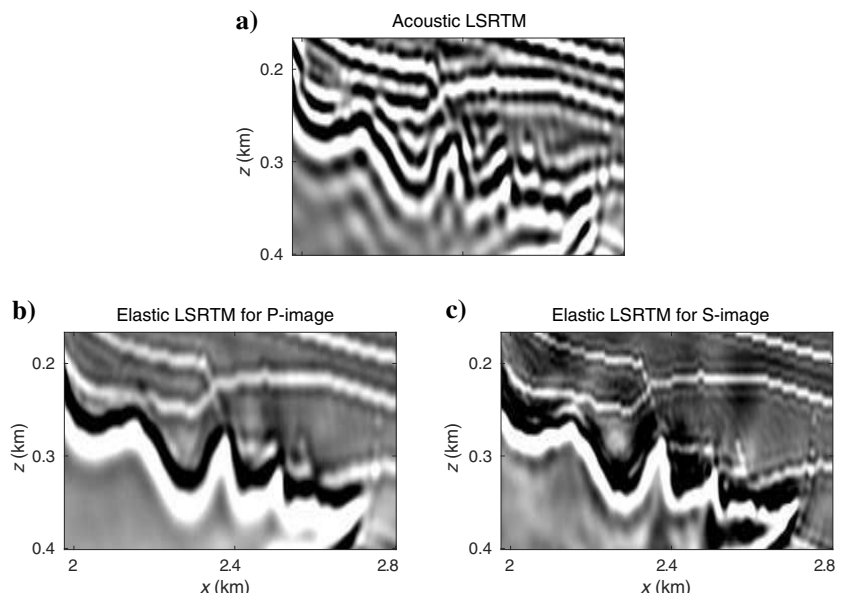
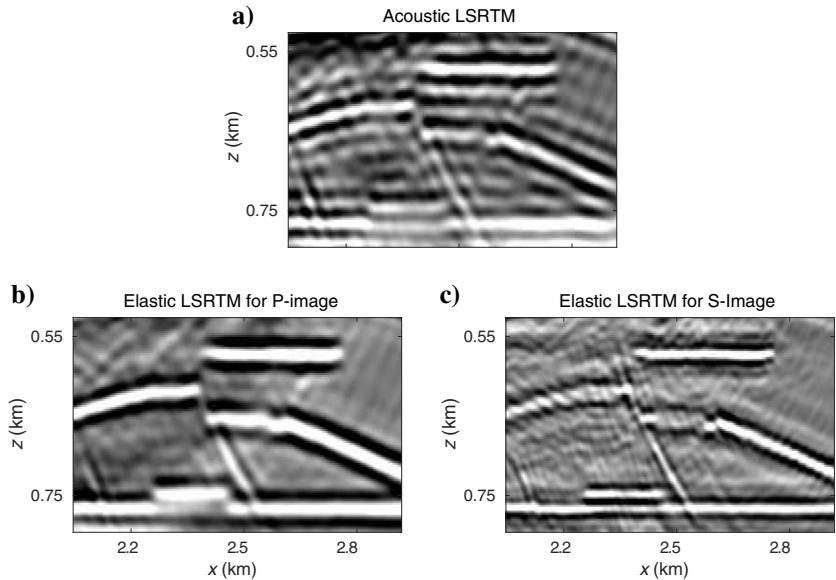


Figure 13. Magnified views of the blue boxes showing the subsalt structures in Figure 10.



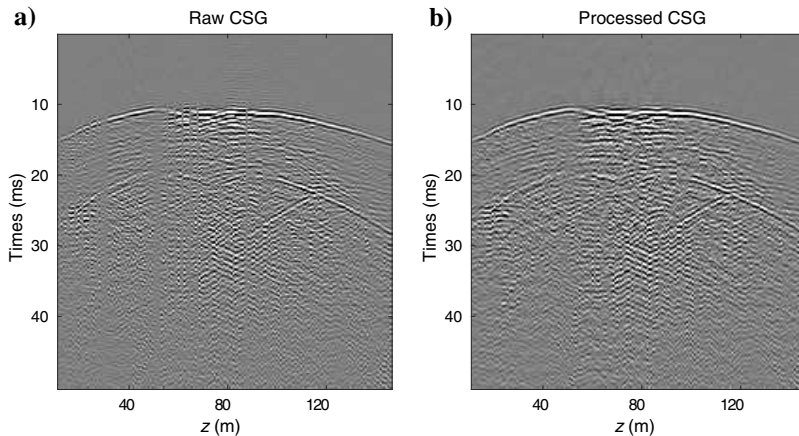


Figure 15. A raw common-shot gather (a) before and (b) after data processing.

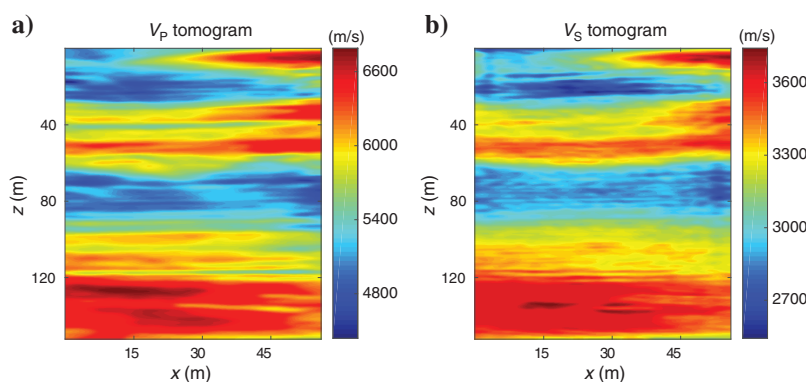


Figure 16. The elastic waveform tomograms for (a) the P- and (b) S-wave velocity distributions.

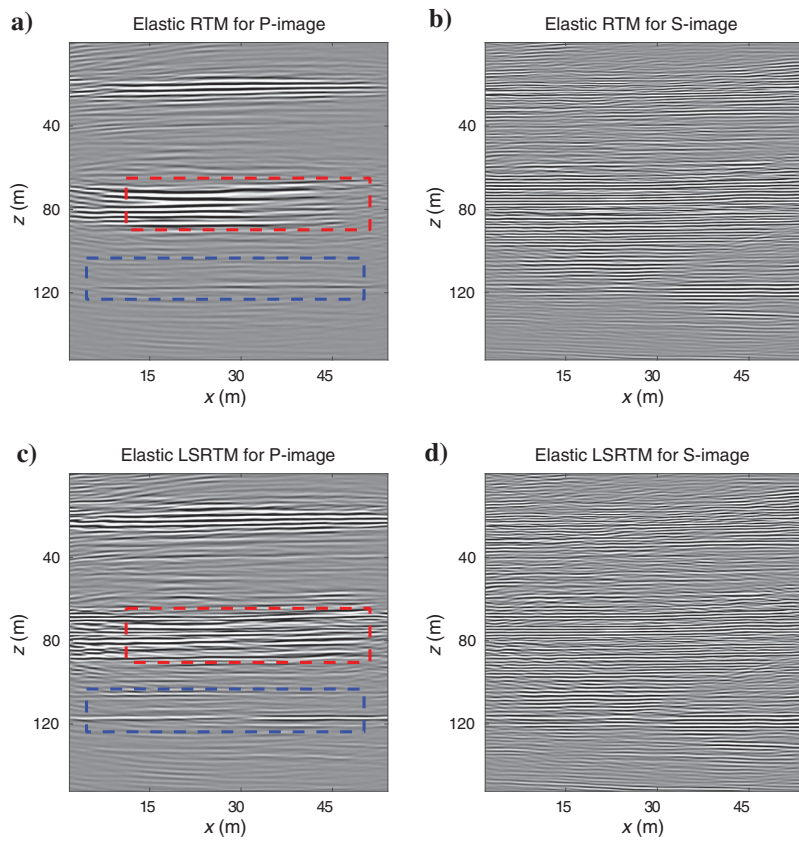


Figure 17. Migration images from elastic RTM (a) for V_P and (b) for V_S , elastic LSRTM (c) for V_P and (d) for V_S .

1997). Also, the P- and S-images suffer from unexpected discontinuity of reflectors and edge effects commonly associated with migrating real crosswell data (Li, 1994; Byun et al., 2002).

DISCUSSION

Previous research has shown that least-squares migration can be quite sensitive to velocity errors (Dutta et al., 2014a; Dutta and Schuster, 2014). This is because the model dimension is smaller than the data dimension, and the data can only be fitted when the background velocity allows for the correct positioning of structures in the image (Hou and Symes, 2016). In the context of elastic LSRTM, accurate background P- and S-wave velocities are needed to relocate the P- and S-wave reflection events back to the correct reflecting interfaces.

In the McElroy crosswell data example, the discontinuity of reflectors in the LSRTM P- and S-images might be caused by an inaccurate

estimate of the P- and S-wave velocities. Because the scattering radiation pattern for δI_S is complex (as shown in Figure 1), the S-image is more sensitive to the velocity errors than the P-image. In addition, the wave-mode crosstalk may degrade the image because the source contains the P- and S-waves, as shown in our source type test. In the crosswell case, the SS reflections are noisy as shown in Figure 15, which hamper the improvement in the S-image. The P-image is improved because δI_P is mostly sensitive to the PP-scattering radiation pattern (as shown in Figure 1), and, compared with the S-image, is less sensitive to noisy data and errors in the assumed velocity model and source-radiation patterns. But still, the S-image can be used to complement the P-image for interpretation purposes.

Another disadvantage of elastic LSRTM is that the computational cost per iteration is an order-of-magnitude more expensive than acoustic RTM. This cost increases linearly with the number of least-squares iterations, but it can be reduced by the multisource migra-

Figure 18. Magnified views of (a and b) the red boxes and (c and d) the blue boxes, in Figure 17a and 17c.

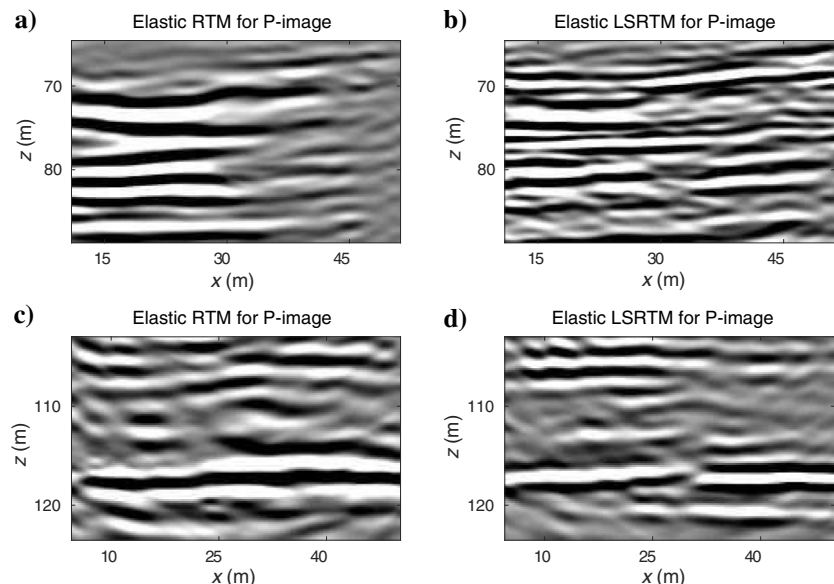
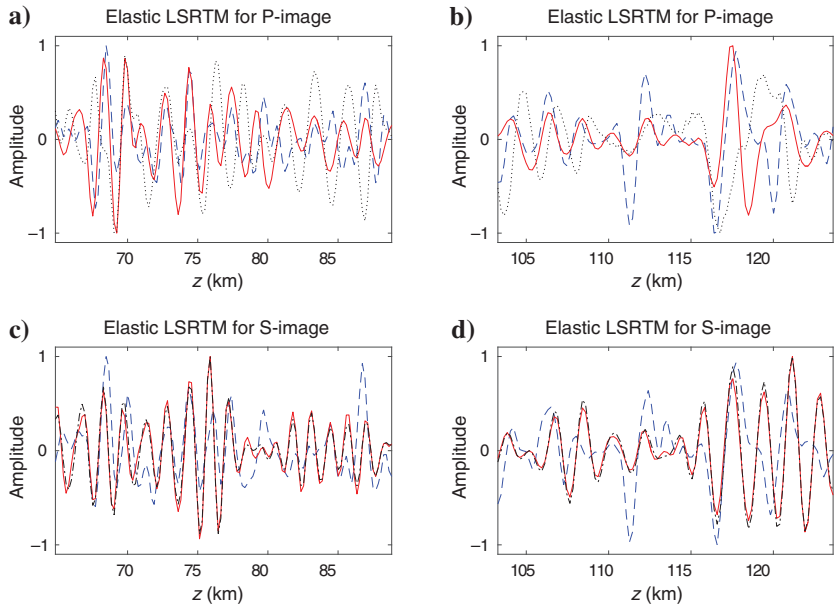


Figure 19. Elastic LSRTM reflectivity profiles (solid red lines) and elastic RTM reflectivity profiles (dotted black line) compared with the P- and S-sonic logs (dashed blue lines) in the receiver well. The profiles are extracted from the elastic LSRTM images (shown in Figures 17c and 19d) 2 m away from the well (a and c) at the depth range of the red boxes and (b and d) at the depth range of the blue boxes, in which the amplitudes have been normalized.



tion methodology (Tang, 2009; Dai and Schuster, 2009; Dai et al., 2011, 2012; Huang and Schuster, 2012).

CONCLUSION

We presented an elastic LSRTM technique to invert for the reflectivity images of P- and S-wave impedances. The proposed formulation can be applied to multicomponent data and can be suitably adjusted to both surface seismic data and crosswell pressure data. It differs from previous formulations of acoustic migration in that elastic LSRTM can handle radiation patterns and migrate events of different wave modes at the same time. Numerical results show that elastic LSRTM can generate images with fewer artifacts, better amplitude balancing, and higher resolution compared with elastic RTM and acoustic LSRTM. Another advantage of elastic LSRTM is that it mitigates the crosstalk problem in elastic RTM. Elastic LSRTM can also improve the imaging of steeply dipping events and generate images with better reflector continuity. Similar to other least-squares migration methods, elastic LSRTM requires an accurate estimation of the P- and S-wave velocity models for migration. Elastic LSRTM also suffers from problems of incorrect estimation of the source radiation patterns.

ACKNOWLEDGMENTS

This research is supported by the King Abdullah University of Science and Technology (KAUST) in Thuwal, Saudi Arabia. We are grateful to the sponsors of the Center for Subsurface Imaging and Modeling Consortium for their financial support. Z. Feng would also like to thank G. Dutta and B. Guo for their help. The computation resource provided by the KAUST Supercomputing Laboratory is greatly appreciated. We are very grateful to Jerry Harris and Robert Langan for the use of the crosswell data set.

APPENDIX A

ADJOINT EQUATION AND GRADIENTS FOR ELASTIC LEAST-SQUARES REVERSE TIME MIGRATION

In matrix-vector notation, equation 1 can be written as (Schuster, 2017)

$$\mathbf{S}\mathbf{w} = \mathbf{F}, \quad (\text{A-1})$$

where

$$\mathbf{S} = \begin{pmatrix} \rho \frac{\partial}{\partial t} & 0 & -\frac{\partial}{\partial x} & 0 & -\frac{\partial}{\partial z} \\ 0 & \rho \frac{\partial}{\partial t} & 0 & -\frac{\partial}{\partial z} & -\frac{\partial}{\partial x} \\ -(\lambda + 2\mu) \frac{\partial}{\partial x} & -\lambda \frac{\partial}{\partial z} & \frac{\partial}{\partial t} & 0 & 0 \\ -\lambda \frac{\partial}{\partial x} & -(\lambda + 2\mu) \frac{\partial}{\partial z} & 0 & \frac{\partial}{\partial t} & 0 \\ -\mu \frac{\partial}{\partial z} & -\mu \frac{\partial}{\partial x} & 0 & 0 & \frac{\partial}{\partial t} \end{pmatrix},$$

$$\mathbf{w} = \begin{pmatrix} u_x \\ u_z \\ \sigma_{xx} \\ \sigma_{zz} \\ \sigma_{xz} \end{pmatrix}, \quad \text{and} \quad \mathbf{F} = \begin{pmatrix} 0 \\ 0 \\ S_{xx} \\ S_{zz} \\ 0 \end{pmatrix}, \quad (\text{A-2})$$

where \mathbf{w} represents the state variables and \mathbf{S} represents the forward modeling operator. The adjoint operator \mathbf{S}^* of \mathbf{S} is given by

$$\mathbf{S}^* = \begin{pmatrix} -\frac{\partial}{\partial t} \rho & 0 & \frac{\partial}{\partial x}(\lambda + 2\mu) & \frac{\partial}{\partial x} \lambda & \frac{\partial}{\partial z} \mu \\ 0 & -\rho \frac{\partial}{\partial t} & \frac{\partial}{\partial z} \lambda & \frac{\partial}{\partial z}(\lambda + 2\mu) & \frac{\partial}{\partial x} \mu \\ \frac{\partial}{\partial x} & 0 & -\frac{\partial}{\partial t} & 0 & 0 \\ 0 & \frac{\partial}{\partial z} & 0 & -\frac{\partial}{\partial t} & 0 \\ \frac{\partial}{\partial z} & \frac{\partial}{\partial x} & 0 & 0 & -\frac{\partial}{\partial t} \end{pmatrix}. \quad (\text{A-3})$$

The L_2 misfit function $\epsilon(\mathbf{m})$ for a model parameter \mathbf{m} can be written as

$$\epsilon(\mathbf{m}) = \frac{1}{2} \|\mathbf{w}(\mathbf{m}) - \mathbf{d}\|^2 = \frac{1}{2} \langle \mathbf{w}(\mathbf{m}) - \mathbf{d}, \mathbf{w}(\mathbf{m}) - \mathbf{d} \rangle, \quad (\text{A-4})$$

where $\mathbf{w}(\mathbf{m})$ and \mathbf{d} represent the predicted and recorded data, respectively, and \mathbf{m} is the predicted model. For a elastic medium, the model parameter \mathbf{m} can be λ , μ , or ρ . The gradient of ϵ is given by

$$\frac{\partial \epsilon(\mathbf{m})}{\partial \mathbf{m}} = \left\langle \frac{\partial \mathbf{w}(\mathbf{m})}{\partial \mathbf{m}}, \mathbf{w}(\mathbf{m}) - \mathbf{d} \right\rangle. \quad (\text{A-5})$$

Taking the derivative of equation A-1, we get

$$\frac{\partial \mathbf{S}(\mathbf{m})}{\partial \mathbf{m}} \mathbf{w}(\mathbf{m}) + \mathbf{S}(\mathbf{m}) \frac{\partial \mathbf{w}(\mathbf{m})}{\partial \mathbf{m}} = 0, \quad (\text{A-6})$$

which can be rearranged to give

$$\frac{\partial \mathbf{w}(\mathbf{m})}{\partial \mathbf{m}} = -\mathbf{S}^{-1}(\mathbf{m}) \frac{\partial \mathbf{S}(\mathbf{m})}{\partial \mathbf{m}} \mathbf{w}(\mathbf{m}). \quad (\text{A-7})$$

Plugging equation A-7 into equation A-5, we get

$$\frac{\partial \epsilon(\mathbf{m})}{\partial \mathbf{m}} = -\left\langle \frac{\partial \mathbf{S}(\mathbf{m})}{\partial \mathbf{m}} \mathbf{w}(\mathbf{m}), (\mathbf{S}(\mathbf{m})^{-1})^* \Delta \mathbf{d} \right\rangle, \quad (\text{A-8})$$

where $*$ denotes the adjoint, $\Delta \mathbf{d} = \mathbf{w}(\mathbf{m}) - \mathbf{d}$ is the residual vector. In the context of elastic LSRTM, we denote $\mathbf{w}(\mathbf{m})^* = (\mathbf{S}(\mathbf{m})^{-1})^* \Delta \mathbf{d}$ as the solution of the adjoint equations with the residual seismograms acting as virtual sources

$$\mathbf{S}^* \mathbf{w}^* = \Delta \mathbf{d}, \quad (\text{A-9})$$

where $\mathbf{w}^* = (\hat{u}_x, \hat{u}_z, \hat{\sigma}_{xx}, \hat{\sigma}_{zz}, \hat{\sigma}_{xz})^T$ is also known as the adjoint-state variables of \mathbf{w} as used in equation 5. If we record the vertical- and horizontal-particle-velocity seismograms, the residual vector $\Delta \mathbf{d}$ can be written as $(\Delta d_x, \Delta d_z, 0, 0, 0)^T$.

For $\mathbf{m} = (\lambda, \mu)^T$, the gradient in equation A-8 can be written as

$$\begin{aligned}\frac{\partial \epsilon}{\partial \lambda} &= -\left\langle \frac{\partial \mathbf{S}}{\partial \lambda} \mathbf{w}, \mathbf{w}^* \right\rangle \\ &= -\left\langle \begin{pmatrix} 0 & 0 & 0 & 0 & 0 \\ 0 & 0 & 0 & 0 & 0 \\ -\frac{\partial}{\partial x} & -\frac{\partial}{\partial z} & 0 & 0 & 0 \\ -\frac{\partial}{\partial x} & -\frac{\partial}{\partial z} & 0 & 0 & 0 \\ 0 & 0 & 0 & 0 & 0 \end{pmatrix} \begin{pmatrix} u_x \\ u_z \\ \sigma_{xx} \\ \sigma_{zz} \\ \sigma_{xz} \end{pmatrix}, \begin{pmatrix} \hat{u}_x \\ \hat{u}_z \\ \hat{\sigma}_{xx} \\ \hat{\sigma}_{zz} \\ \hat{\sigma}_{xz} \end{pmatrix} \right\rangle \\ &= \int_0^T \left(\frac{\partial u_x}{\partial x} + \frac{\partial u_z}{\partial z} \right) (\hat{\sigma}_{xx} + \hat{\sigma}_{zz}) dt, \quad (\text{A-10})\end{aligned}$$

and

$$\begin{aligned}\frac{\partial \epsilon}{\partial \mu} &= -\left\langle \frac{\partial \mathbf{S}}{\partial \mu} \mathbf{w}, \mathbf{w}^* \right\rangle \\ &= -\left\langle \begin{pmatrix} 0 & 0 & 0 & 0 & 0 \\ 0 & 0 & 0 & 0 & 0 \\ -2\frac{\partial}{\partial x} & 0 & 0 & 0 & 0 \\ 0 & -2\frac{\partial}{\partial z} & 0 & 0 & 0 \\ -\frac{\partial}{\partial z} & -\frac{\partial}{\partial x} & 0 & 0 & 0 \end{pmatrix} \begin{pmatrix} u_x \\ u_z \\ \sigma_{xx} \\ \sigma_{zz} \\ \sigma_{xz} \end{pmatrix}, \begin{pmatrix} \hat{u}_x \\ \hat{u}_z \\ \hat{\sigma}_{xx} \\ \hat{\sigma}_{zz} \\ \hat{\sigma}_{xz} \end{pmatrix} \right\rangle \\ &= \int_0^T 2 \left(\frac{\partial u_x}{\partial x} \hat{\sigma}_{xx} + \frac{\partial u_z}{\partial z} \hat{\sigma}_{zz} \right) + \left(\frac{\partial u_x}{\partial z} + \frac{\partial u_z}{\partial x} \right) \hat{\sigma}_{xz} dt. \quad (\text{A-11})\end{aligned}$$

REFERENCES

- Anikiev, D., B. Kashtan, and W. A. Mulder, 2013, Decoupling of elastic parameters with iterative linearized inversion: 73rd Annual International Meeting, SEG, Expanded Abstracts, 3185–3190.
- Brenders, A. J., and R. G. Pratt, 2007, Full waveform tomography for lithospheric imaging: Results from a blind test in a realistic crustal model: *Geophysical Journal International*, **168**, 133–151.
- Byun, J., J. W. Rector, III, and T. Nemeth, 2002, Postmap migration of crosswell reflection seismic data: *Geophysics*, **67**, 135–146, doi: [10.1190/1.1451423](https://doi.org/10.1190/1.1451423).
- Chang, W., and G. A. McMechan, 1987, Elastic reverse time migration: *Geophysics*, **52**, 1365–1375, doi: [10.1190/1.1442249](https://doi.org/10.1190/1.1442249).
- Chavent, G., and R.-E. Plessix, 1999, An optimal true-amplitude least-squares prestack depth-migration operator: *Geophysics*, **64**, 508–515, doi: [10.1190/1.1444557](https://doi.org/10.1190/1.1444557).
- Crase, E., A. Pica, M. Noble, J. McDonald, and A. Tarantola, 1990, Robust elastic nonlinear waveform inversion: Application to real data: *Geophysics*, **55**, 527–538, doi: [10.1190/1.1442864](https://doi.org/10.1190/1.1442864).
- Dai, W., P. Fowler, and G. T. Schuster, 2012, Multi-source least-squares reverse time migration: *Geophysical Prospecting*, **60**, 681–695, doi: [10.1111/j.1365-2478.2012.01092.x](https://doi.org/10.1111/j.1365-2478.2012.01092.x).
- Dai, W., and J. Schuster, 2009, Least-squares migration of simultaneous sources data with a deblurring filter: 79th Annual International Meeting, SEG, Expanded Abstracts, 2990–2994, doi: [10.1190/1.3255474](https://doi.org/10.1190/1.3255474).
- Dai, W., and G. T. Schuster, 2013, Plane-wave least-squares reverse-time migration: *Geophysics*, **78**, no. 4, S165–S177, doi: [10.1190/geo2012-0377.1](https://doi.org/10.1190/geo2012-0377.1).
- Dai, W., X. Wang, and G. T. Schuster, 2011, Least-squares migration of multi-source data with a deblurring filter: *Geophysics*, **76**, no. 5, R135–R146, doi: [10.1190/geo2010-0159.1](https://doi.org/10.1190/geo2010-0159.1).
- Dai, W., Z. Xu, and R. Coates, 2015, Least-squares reverse-time migration for visco-acoustic media: 85th Annual International Meeting, SEG, Expanded Abstracts, 3387–3391.
- Du, Q., Y. Zhu, and J. Ba, 2012, Polarity reversal correction for elastic reverse time migration: *Geophysics*, **77**, no. 2, S31–S41, doi: [10.1190/geo2011-0348.1](https://doi.org/10.1190/geo2011-0348.1).
- Duan, Y., and P. Sava, 2015, Scalar imaging condition for elastic reverse time migration: *Geophysics*, **80**, no. 4, S127–S136, doi: [10.1190/geo2014-0453.1](https://doi.org/10.1190/geo2014-0453.1).
- Duquet, B., K. J. Marfurt, and J. A. Dellinger, 2000, Kirchhoff modeling, inversion for reflectivity, and subsurface illumination: *Geophysics*, **65**, 1195–1209, doi: [10.1190/1.1444812](https://doi.org/10.1190/1.1444812).
- Dutta, G., Y. Huang, W. Dai, X. Wang, and G. T. Schuster, 2014a, Making the most out of the least (squares migration): 84th Annual International Meeting, SEG, Expanded Abstracts, 4405–4410.
- Dutta, G., and G. T. Schuster, 2014, Attenuation compensation for least-squares reverse time migration using the viscoacoustic-wave equation: *Geophysics*, **79**, no. 6, S251–S262, doi: [10.1190/geo2013-0414.1](https://doi.org/10.1190/geo2013-0414.1).
- Dutta, G., M. Sinha, and G. T. Schuster, 2014b, A cross-correlation objective function for least-squares migration and visco-acoustic imaging: 84th Annual International Meeting, SEG, Expanded Abstracts, 3985–3990.
- Etgen, J. T., 1988, Prestacked migration of P and SV-waves: 66th Annual International Meeting, SEG, Expanded Abstracts, 972–975.
- Granli, J. R., B. Arntsen, A. Sollid, and E. Hilde, 1999, Imaging through gas-filled sediments using marine shear-wave data: *Geophysics*, **64**, 668–677, doi: [10.1190/1.1444576](https://doi.org/10.1190/1.1444576).
- Guasch, L., M. Warner, T. Nangoo, J. Morgan, A. Umpleby, I. Stekl, and N. Shah, 2012, Elastic 3D full-waveform inversion: 82nd Annual International Meeting, SEG, Expanded Abstracts, doi: [10.1190/segam2012-1239.1](https://doi.org/10.1190/segam2012-1239.1).
- Harris, J. M., R. C. NolenHoeksema, R. T. Langan, M. V. Schaack, S. K. Lazaratos, and J. W. Rector, 1995, High resolution crosswell imaging of a West Texas carbonate reservoir. Part 1: Project summary and interpretation: *Geophysics*, **60**, 667–681, doi: [10.1190/1.1443806](https://doi.org/10.1190/1.1443806).
- Hokstad, K., 2000, Multicomponent Kirchhoff migration: *Geophysics*, **65**, 861–873, doi: [10.1190/1.1444783](https://doi.org/10.1190/1.1444783).
- Hou, J., and W. W. Symes, 2016, Accelerating extended least-squares migration with weighted conjugate gradient iteration: *Geophysics*, **81**, no. 4, S165–S179, doi: [10.1190/geo2015-0499.1](https://doi.org/10.1190/geo2015-0499.1).
- Huang, Y., and G. T. Schuster, 2012, Multisource least-squares migration of marine streamer data with frequency-division encoding: *Geophysics*, **60**, 663–680.
- Jiao, K., W. Huang, D. Vigh, J. Kapoor, R. Coates, E. W. Starr, and X. Cheng, 2012, Elastic migration for improving salt and subsalt imaging and inversion: 82nd Annual International Meeting, SEG, Expanded Abstracts, doi: [10.1190/segam2012-0791.1](https://doi.org/10.1190/segam2012-0791.1).
- Kaplan, S. T., P. S. Routh, and M. D. Sacchi, 2010, Derivation of forward and adjoint operators for least-squares shot-profile split-step migration: *Geophysics*, **75**, no. 6, S225–S235, doi: [10.1190/1.3506146](https://doi.org/10.1190/1.3506146).
- Kuhl, H., and M. D. Sacchi, 2003, Least squares wave-equation migration for AVP/AVA inversion: *Geophysics*, **68**, 262–273, doi: [10.1190/1.1543212](https://doi.org/10.1190/1.1543212).
- Kuo, J. T., and T. Dai, 1984, Kirchhoff elastic wave migration for the case of noncoincident source and receiver: *Geophysics*, **49**, 1223–1238, doi: [10.1190/1.1441751](https://doi.org/10.1190/1.1441751).
- Kurkjian, A. L., H. Schmidt, T. L. Marzetta, J. E. White, and C. Chouzenoux, 1992, Numerical modeling of crosswell seismic monopole sensor data: 60th Annual International Meeting, SEG, Expanded Abstracts, 141–144.
- Lailly, P., 1984, Migration methods: Partial but efficient solutions to the seismic inverse problem: *Inverse Problems of Acoustic and Elastic Waves*, **51**, 13871403.
- Levander, A. R., 1988, Fourth-order finite-difference P-SV seismograms: *Geophysics*, **53**, 1425–1436, doi: [10.1190/1.1442422](https://doi.org/10.1190/1.1442422).
- Li, G., 1994, Crosswell seismic processing: Automatic velocity analysis, filtering, and reflection imaging: Ph.D. thesis, University of Calgary.
- Lu, R., P. Traynin, and J. E. Anderson, 2009, Comparison of elastic and acoustic reverse time migration on the synthetic elastic Marmousi OBC dataset: 79th Annual International Meeting, SEG, Expanded Abstracts, 2799–2803.
- Mora, P., 1987, Nonlinear two-dimensional elastic inversion of multioffset seismic data: *Geophysics*, **52**, 1211–1228, doi: [10.1190/1.1442384](https://doi.org/10.1190/1.1442384).
- Mora, P., 1988, Elastic wave-field inversion of reflection and transmission data: *Geophysics*, **53**, 750–759, doi: [10.1190/1.1442510](https://doi.org/10.1190/1.1442510).
- Nemeth, T., C. Wu, and G. T. Schuster, 1999, Least-squares migration of incomplete reflection data: *Geophysics*, **64**, 208–221, doi: [10.1190/1.1444517](https://doi.org/10.1190/1.1444517).
- Nocedal, J., and S. J. Wright, 1999, *Numerical optimization*: Springer.
- Plessix, R.-E., 2006, A review of the adjoint-state method for computing the gradient of a functional with geophysical applications: *Geophysical Journal International*, **167**, 495–503, doi: [10.1111/j.1365-246X.2006.02978.x](https://doi.org/10.1111/j.1365-246X.2006.02978.x).
- Plessix, R.-E., and W. A. Mulder, 2004, Frequency-domain finite-difference amplitude-preserving migration: *Geophysical Journal International*, **157**, 975–987, doi: [10.1111/j.1365-246X.2004.02282.x](https://doi.org/10.1111/j.1365-246X.2004.02282.x).
- Prieux, V., R. Brossier, S. Operto, and J. Virieux, 2013, Multiparameter full waveform inversion of multicomponent ocean-bottom-cable data from the valhall field. Part 2: Imaging compressive-wave and shear-wave velocities: *Geophysical Journal International*, **194**, 1665–1681, doi: [10.1093/gji/gji178](https://doi.org/10.1093/gji/gji178).

- Raknes, E., and B. Arntsen, 2014, Strategies for elastic full waveform inversion: 84th Annual International Meeting, SEG, Expanded Abstracts, 1222–1226.
- Ravaut, C., S. Operto, L. Imrota, J. Virieux, A. Herrero, and P. Dell'Aversana, 2004, Multiscale imaging of complex structures from multifold wide-aperture seismic data by frequency-domain full-waveform tomography: Application to a thrust belt: *Geophysical Journal International*, **159**, 1032–1056, doi: [10.1111/j.1365-246X.2004.02442.x](https://doi.org/10.1111/j.1365-246X.2004.02442.x).
- Sears, T., S. Singh, and P. Barton, 2008, Elastic full waveform inversion of multi-component OBC seismic data: *Geophysical Prospecting*, **56**, 843–862, doi: [10.1111/j.1365-2478.2008.00692.x](https://doi.org/10.1111/j.1365-2478.2008.00692.x).
- Sears, T. J., P. J. Barton, and S. C. Singh, 2010, Elastic full waveform inversion of multicomponent ocean-bottom cable seismic data: Application to Alba field, U.K. North Sea: *Geophysics*, **75**, no. 6, R109–R119, doi: [10.1190/1.3484097](https://doi.org/10.1190/1.3484097).
- Schuster, G. T., 2017, Seismic inversion: SEG.
- Sinha, M., and G. T. Schuster, 2015, Mitigation of defocusing by statics and near-surface velocity errors by interferometric least-squares migration: 75th Annual International Meeting, SEG, Expanded Abstracts, 4254–4258.
- Stanton, A., and M. D. Sacchi, 2014, Least squares migration of converted wave seismic data: *CSEG Recorder*, **39**, 48–52.
- Stanton, A., and M. D. Sacchi, 2015, Least-squares wave-equation migration of elastic data: 77th Annual International Conference and Exhibition, EAGE, Extended Abstracts, Tu N116 106.
- Stewart, R. R., J. E. Gaiser, R. J. Brown, and D. C. Lawton, 2002, Converted wave seismic exploration: Methods: *Geophysics*, **67**, 1348–1363, doi: [10.1190/1.1512781](https://doi.org/10.1190/1.1512781).
- Stewart, R. R., J. E. Gaiser, R. J. Brown, and D. C. Lawton, 2003, Converted wave seismic exploration: Applications: *Geophysics*, **68**, 40–57, doi: [10.1190/1.1543193](https://doi.org/10.1190/1.1543193).
- Sun, R., and G. A. McMechan, 2001, Scalar reverse time depth migration of prestack elastic seismic data: *Geophysics*, **66**, 1519–1527, doi: [10.1190/1.1487098](https://doi.org/10.1190/1.1487098).
- Tang, Y., 2009, Target-oriented wave-equation least-squares migration/inversion with phase-encoded Hessian: *Geophysics*, **74**, no. 6, WCA95–WCA107, doi: [10.1190/1.3204768](https://doi.org/10.1190/1.3204768).
- Tarantola, A., 1984, Inversion of seismic reflection data in the acoustic approximation: *Geophysics*, **49**, 1259–1266, doi: [10.1190/1.1441754](https://doi.org/10.1190/1.1441754).
- Tarantola, A., 1986, A strategy for nonlinear elastic inversion of seismic reflection data: *Geophysics*, **51**, 1893–1903, doi: [10.1190/1.1442046](https://doi.org/10.1190/1.1442046).
- Valenciano, A. A., B. Biondi, and A. Guittot, 2006, Target-oriented wave-equation inversion: *Geophysics*, **71**, no. 4, A35–A38, doi: [10.1190/1.2213359](https://doi.org/10.1190/1.2213359).
- Virieux, J., and S. Operto, 2009, An overview of full-waveform inversion in exploration geophysics: *Geophysics*, **74**, no. 6, WCC1–WCC26, doi: [10.1190/1.3238367](https://doi.org/10.1190/1.3238367).
- White, J. E., and M. A. Lessenger, 1988, Caliper effect on borehole coupling: *Exploration Geophysics*, **19**, 201–205, doi: [10.1071/EG988201](https://doi.org/10.1071/EG988201).
- Wu, R., and K. Aki, 1985, Scattering characteristics of elastic waves by an elastic heterogeneity: *Geophysics*, **50**, 582–595, doi: [10.1190/1.1441934](https://doi.org/10.1190/1.1441934).
- Yan, J., and P. Sava, 2008, Isotropic angle-domain elastic reverse-time migration: *Geophysics*, **73**, no. 6, S229–S239, doi: [10.1190/1.2981241](https://doi.org/10.1190/1.2981241).
- Zeng, C., S. Dong, and B. Wang, 2013, Least-squares reverse time migration: Inversion-based imaging toward true reflectivity: *The Leading Edge*, **33**, 962–964, 966, 968, doi: [10.1190/tle33090962.1](https://doi.org/10.1190/tle33090962.1).
- Zhang, Y., L. Duan, and Y. Xie, 2013, A stable and practical implementation of least-squares reverse time migration: 83rd Annual International Meeting, SEG, Expanded Abstracts, 3716–3720.
- Zhang, Y., L. Duan, and Y. Xie, 2015, A stable and practical implementation of least-squares reverse time migration: *Geophysics*, **80**, no. 1, V23–V31, doi: [10.1190/geo2013-0461.1](https://doi.org/10.1190/geo2013-0461.1).
- Zhe, J., and S. A. Greenhalgh, 1997, Prestack multicomponent migration: *Geophysics*, **62**, 598–613, doi: [10.1190/1.1444169](https://doi.org/10.1190/1.1444169).
- Zhou, C., G. T. Schuster, S. Hassanzadeh, and J. M. Harris, 1997, Elastic wave equation traveltime and waveform inversion of crosswell data: *Geophysics*, **62**, 853–868, doi: [10.1190/1.1444194](https://doi.org/10.1190/1.1444194).